The Astronomical Journal, 136:498–505, 2008 July doi:10.1088/0004-6256/136/1/498

HUBBLE SPACE TELESCOPE IMAGING OF BRIGHT LYMAN BREAK GALAXY CANDIDATES FROM THE SLOAN DIGITAL SKY SURVEY: NOT LBGS AFTER ALL

Misty C. Bentz[1], Richard W. Pogge, and Patrick S. Osmer
Department of Astronomy, The Ohio State University, 140 West 18th Avenue, Columbus, OH 43210, USA; mbentz@uci.edu, pogge@astronomy.ohio-state.edu, and osmer@astronomy.ohio-state.edu
Received 2008 January 22; accepted 2008 May 6; published 2008 June 13

ABSTRACT

We present deep *Hubble Space Telescope* ACS and NICMOS images of six bright Lyman break galaxy candidates that were previously discovered in the Sloan Digital Sky Survey. We find that five of the objects are consistent with unresolved point sources. Although somewhat atypical of the class, they are most likely LoBAL quasars, perhaps FeLoBALs. The sixth object, J1147, has a faint companion galaxy located ∼0.8 arcsec to the southwest. The companion contributes ∼8% of the flux in the observed-frame optical and infrared. It is unknown whether this companion is located at the same redshift as J1147.

Key words: galaxies: active – galaxies: high-redshift – galaxies: photometry

1. INTRODUCTION

The discovery of an apparently luminous ($r \approx 20.5$ mag) star-forming galaxy at $z \approx 2.5$ by Bentz & Osmer (2004) in the Early Data Release (EDR, Stoughton et al. 2002) of the Sloan Digital Sky Survey (SDSS, York et al. 2000) Quasar Catalog (Schneider et al. 2002) was an unexpected surprise. Most known Lyman break galaxies (LBGs) have been discovered in deep images covering very small areas of the sky, and the brightest LBGs have $R_{AB} \approx 23$ mag, which is much fainter than the limit of the SDSS. A dedicated search through the SDSS First Data Release (DR1, Abazajian et al. 2003) produced five additional objects, as well as the original EDR object (Bentz et al. 2004, see Figure 1), with redshifts $2.45 < z < 2.80$ and $19.8 < m_r < 20.5$. These six objects, by definition, have similar emission- and absorption-line properties to the LBG composite spectrum produced from 811 individual objects (Shapley et al. 2003), but there are slight differences as well, in that the spectra are redder, the widths of the lines are greater, and the high-ionization lines are stronger than the lower-ionization lines. While such differences bring into question the true nature of the underlying source of power for these objects, the different possibilities are all extremely important.

The first possibility is that these objects truly are ultraluminous LBGs, over 4 mag brighter than an "L_*" LBG. Using the continuum luminosity at λ1500 as a proxy for the star formation, Bentz et al. (2004) calculated the star-formation rates (SFRs) to be ∼300–1000 $M_\odot$ yr^{-1}, *without* corrections for dust. As these spectra are quite red, the amount of light attenuated by dust can be expected to be higher than the typical factor of 7 determined by Shapley et al. (2003) for LBGs, which would indicate significantly higher SFRs. The turbulence of such a system may be able to reproduce the differences observed in the spectra of the objects compared to the composite spectrum. A rough estimate of the luminosity function of these objects is well above a Schechter (1976) function extrapolation of the LBG luminosity function determined by Adelberger & Steidel (2000). Such objects would be the most luminous members of their class known, and would be extremely important in understanding the formation and evolution of star-forming galaxies at their peak epoch of $z \approx 3$. Furthermore, because the space density of these objects is higher than predicted, they could represent a new class of objects or activity.

The second possibility is that these objects are star-forming galaxies, but they are significantly brightened by gravitational lensing. This has already been found to be the case with the galaxy MS 1512-cB58, which is an "L_*" LBG magnified by a factor of 30 by a foreground cluster (Seitz et al. 1998). The lensing hypothesis would account for the space density being higher than predicted for objects this luminous, but it does not seem to be borne out by the differences in the spectra of the objects when compared with the LBG composite of Shapley et al. (2003).

Finally, it is possible that these objects are an unusual class of active galactic nuclei (AGNs) that has not been previously seen. The greater line widths in the spectra of the candidates when compared with the composite spectrum could be evidence for the AGN hypothesis, and one object has a hint of a broad C III emission line. The main argument against this hypothesis has been the high level of similarity between the spectra of the objects and the LBG composite spectrum.

With the SDSS data alone, the exact mechanism behind the source of power in these objects cannot be determined. While there is no evidence for lensing in the SDSS images, and the fields surrounding the objects seem quite empty, groups or clusters at $z \approx 1$ would be too faint to be detected by the SDSS. Also, the typical point-spread function (PSF) of the SDSS images is ∼1.4″, which would mask any distortions of the source caused by gravitational lensing, and also effectively confuses the distinction between a point source or an extended object with a diameter on the scale of the PSF. Furthermore, the low signal-to-noise ratio (S/N) of the SDSS spectra masks the finer details in the rest-frame UV spectra and thus prevents a decision on whether the source of power is dominated by star formation or AGN emission.

In this paper, we present deep *Hubble Space Telescope* (*HST*) follow-up images of these six candidates discovered by Bentz et al. (2004) in the rest-frame UV and optical. We apply two-dimensional image decomposition techniques to determine the morphological classifications of each of the objects and the relative contributions of the fitted components to the flux of each object. We find that five of the objects are consistent with unresolved point sources (i.e., AGNs), and that the sixth has a

[1] Present address: Department of Physics and Astronomy, 4129 Frederick Reines Hall, University of California, Irvine, CA 92697, USA.

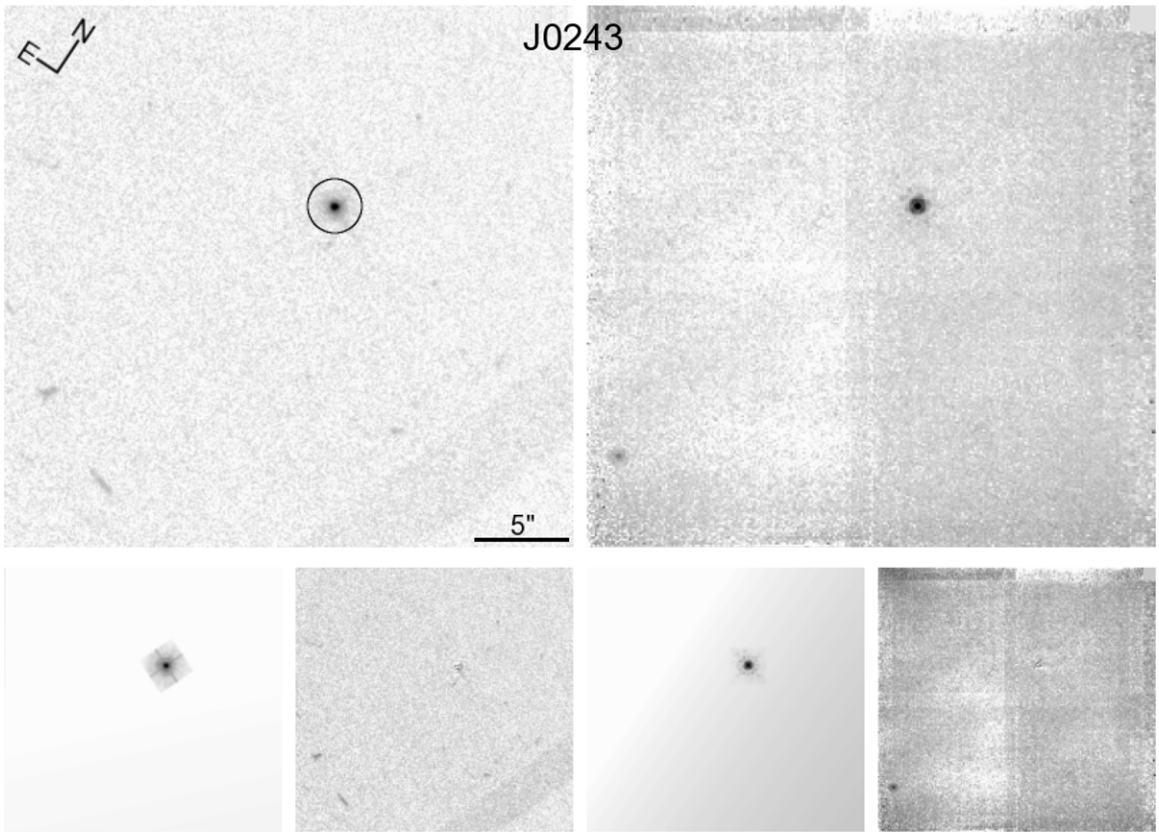

Figure 1. ACS imaging of J0243 through the F625W filter (top left panel) and NICMOS imaging of J0243 through the F160W filter (top right panel). The circle around the object in the ACS image shows the size of the SDSS fiber on the sky. The ACS images have been scaled and oriented to match the NICMOS images. The bottom panels show, from left to right: Galfit model of the ACS image and any field objects that appear in both the optical and infrared, Galfit residuals after subtracting the model from the ACS image, Galfit model of the NICMOS image of J0243 and any shared field objects, and Galfit residuals after subtracting the model from the NICMOS image.

faint, nearby companion that contributes ∼8% of the rest-frame UV flux measured through the SDSS fiber. Finally, we discuss the results of our analysis in the context of additional follow-up studies that have meanwhile been carried out on these unusual objects.

2. OBSERVATIONS

Each of the six candidate bright LBGs listed in Table 1 were observed for a total of three orbits with the *HST*: two orbits with the Advanced Camera for Surveys Wide-Field Channel (ACS WFC), and one orbit with the Near-Infrared Camera and Multi-Object Spectrometer (NICMOS). With the ACS WFC we acquired deep r-band images with the goal of studying the rest-frame UV morphology of the objects, and to search for evidence of possible foreground lensing of the objects. Deep H-band images with the NICMOS NIC2 camera were acquired to try to detect the host galaxy in the rest-frame optical, as well as to search for any nearby galaxies in proximity to our primary targets. We present the details of the observations for each in the following sections.

2.1. Advanced Camera for Surveys

Each of the six targets was observed with two full *HST* orbits using the ACS WFC through the F625W filter (similar to the SDSS r filter). The F625W filter was chosen specifically to take advantage of the maximum throughput of the optics at 6300 Å to get deep images of the fields in the rest-frame UV and any foreground groups or clusters. The higher sensitivity of the WFC was deemed more important in this case than the resolution that would be afforded by the High Resolution Channel on the ACS. Table 1 lists the total exposure time for each object, which was broken up into five individual exposures of ∼14 min each. Between each of the five exposures, the telescope was dithered in a line pattern, with a typical offset of 3 arcsec per dither, to assist in the rejection of cosmic rays and bad pixels.

The standard *HST* reduction and calibration pipeline did a fine job of processing and combining the individual images, which are presented in the left hand panels of Figures 1–6, rotated and scaled to match the field of view of NICMOS.

2.2. Near-Infrared Camera and Multi-Object Spectrometer

Each of the six objects was also observed for one full orbit with the NIC2 camera on NICMOS through the F160W (broad-band H) filter. The observations were scheduled to avoid the cosmic ray persistence problem caused by the South Atlantic Anomaly.[2] The F160W filter was chosen to take advantage of the fact that the rest-frame visible spectrum is redshifted into the infrared and would be the best way to study any visible hosts and companions of our targets.

The observations were acquired in MULTIACCUM mode, utilizing the *step64* sample sequence, which has a series of rapid, non-destructive reads up to 64 s, and then reads out in steps of 64 s. Such a sample sequence gives a high dynamic range in the resulting image, which allows for the study of both

[2] See ISR NICMOS-98-001.

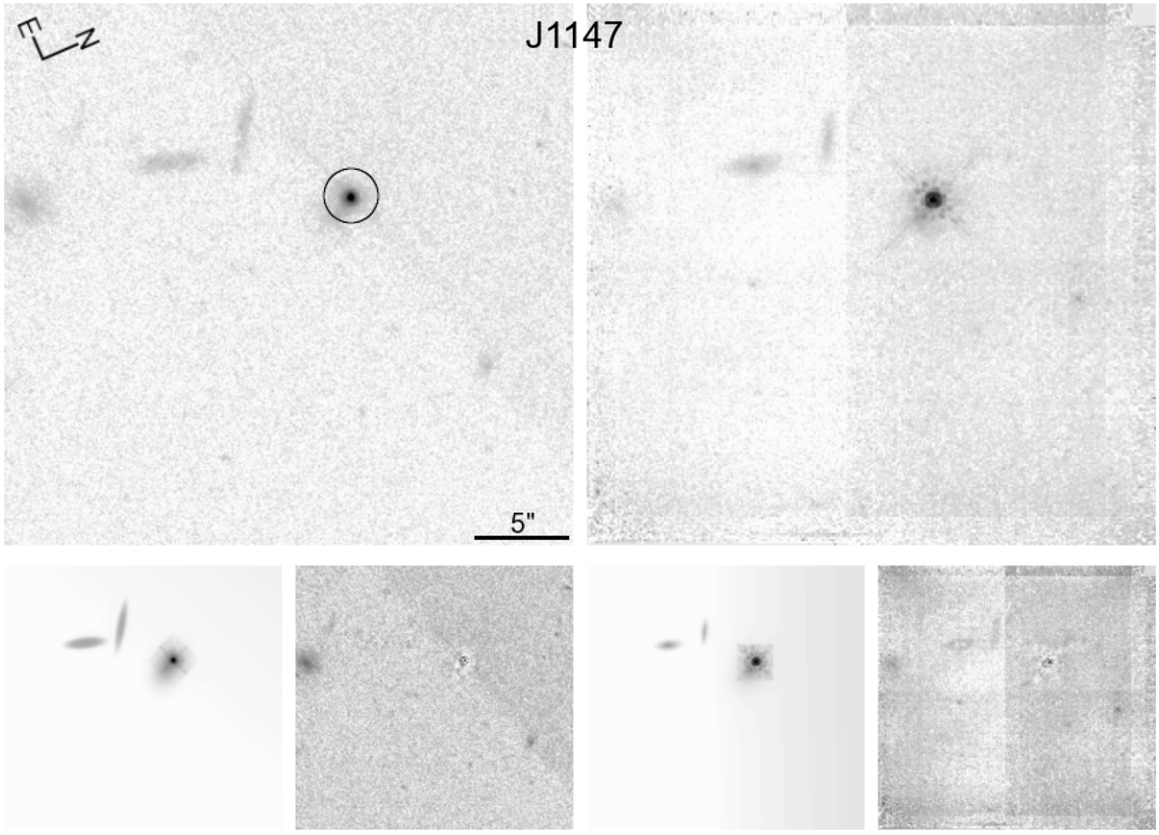

Figure 2. Same as Figure 1, but for J1147. Note the additional flux component located to the southwest of the PSF.

Table 1
Observation Log

Object	z	ACS WFC F625W		NIC2 F160W	
(SDSS J)		Date observed (yyyy-mm-dd)	Exp. time (s)	Date observed (yyyy-mm-dd)	Exp. time (s)
024343.77−082109.9	2.590	2005-01-11	4150.0	2004-08-12	2559.7
114756.00−025023.5	2.556	2004-11-20	4150.0	2004-11-19	3046.4
134026.44+634433.2	2.786	2004-07-12	4550.0	2004-07-24	2687.7
143224.55−000116.4	2.472	2005-12-27	4000.0	2004-08-12	2559.7
144424.55+013457.0	2.670	2005-01-10	4150.0	2004-08-12	2559.7
155359.96+005641.3	2.635	2006-03-09	4150.0	2004-08-12	2559.7

very faint and very bright objects in the same field. The total exposure time for each target is listed in Table 1, and is typically composed of five separate exposures of 511 s. For J1147 we were able to acquire two additional exposure of 243 s, and for J1340, a total of seven exposures of 384 s each were acquired. Between each individual exposure, the spacecraft was dithered in a spiral pattern, with a typical offset of 1 arcsec.

The images were reduced and combined in the usual way by the *HST* calibration pipeline, and are presented in the right-hand panels of Figures 1–6.

3. IMAGE DECOMPOSITIONS

At first glance, all six of the objects appear to be unresolved in both the rest-frame UV and optical, although there does appear to be a faint companion to J1147 that is slightly offset from the PSF of the unresolved target. Within a radius of ∼20 arcsec, the fields of these objects appear rather unremarkable, although there may be a slight overdensity in the field of J1432.

To search for any faint host galaxy contribution that may be hiding underneath the bright PSF, we employed the two-dimensional image decomposition program Galfit (Peng et al. 2002), which fits analytic functions to an image, convolved with a user-supplied PSF model. Model PSFs were created using the TinyTim software package, which models the optics of *HST* plus the specifics of the camera and filter system (Krist 1993). For the ACS images, a model PSF was created for the location of the target in each individual exposure, and the model PSFs were then drizzled together and corrected for the distortion in the optics of the camera using the same methods as were applied to the data.

As each of the targets is very compact and the fields are relatively empty, we initially fit the images of each target with a central PSF and a sky background that was allowed to tilt. This simple model gives a reasonable fit to both the ACS and NICMOS image of each target, except for J1147, which clearly has a faint companion offset a few pixels (∼0.8 arcsec) to the southwest of center of the PSF. However, in all cases, a slightly

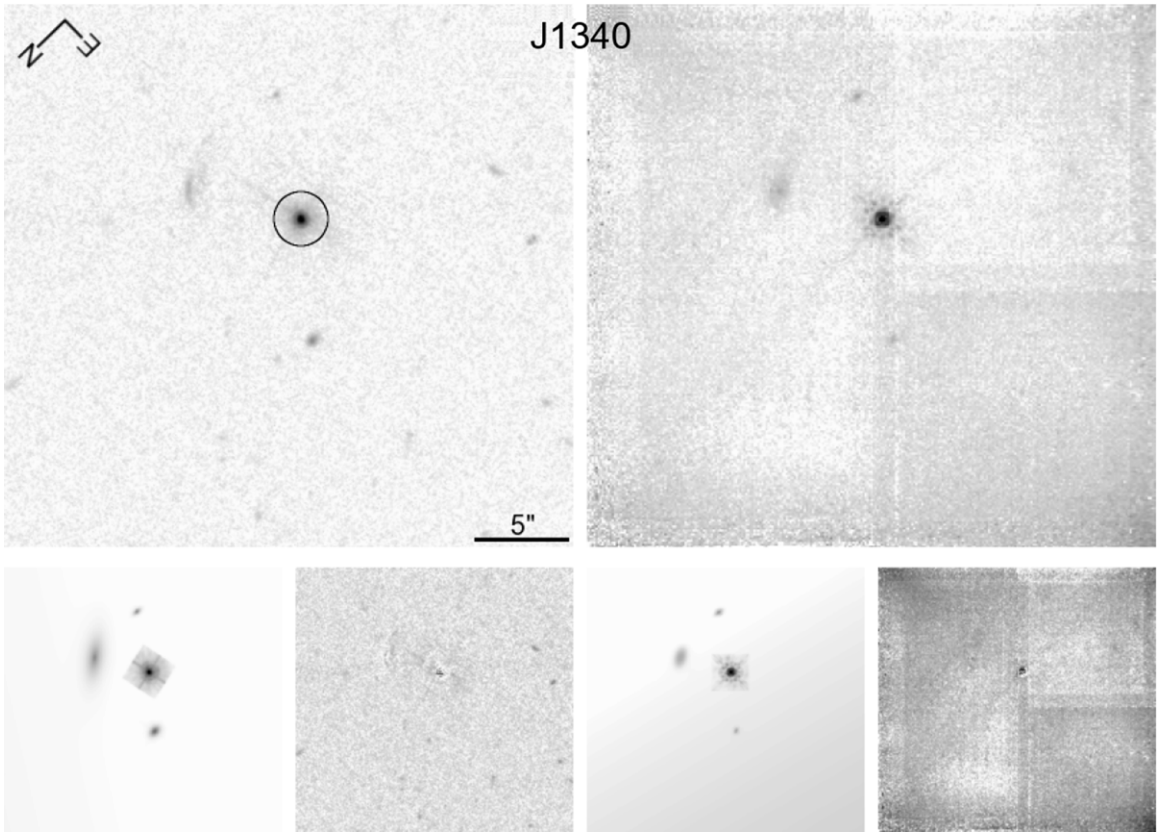

Figure 3. Same as Figure 1, but for J1340.

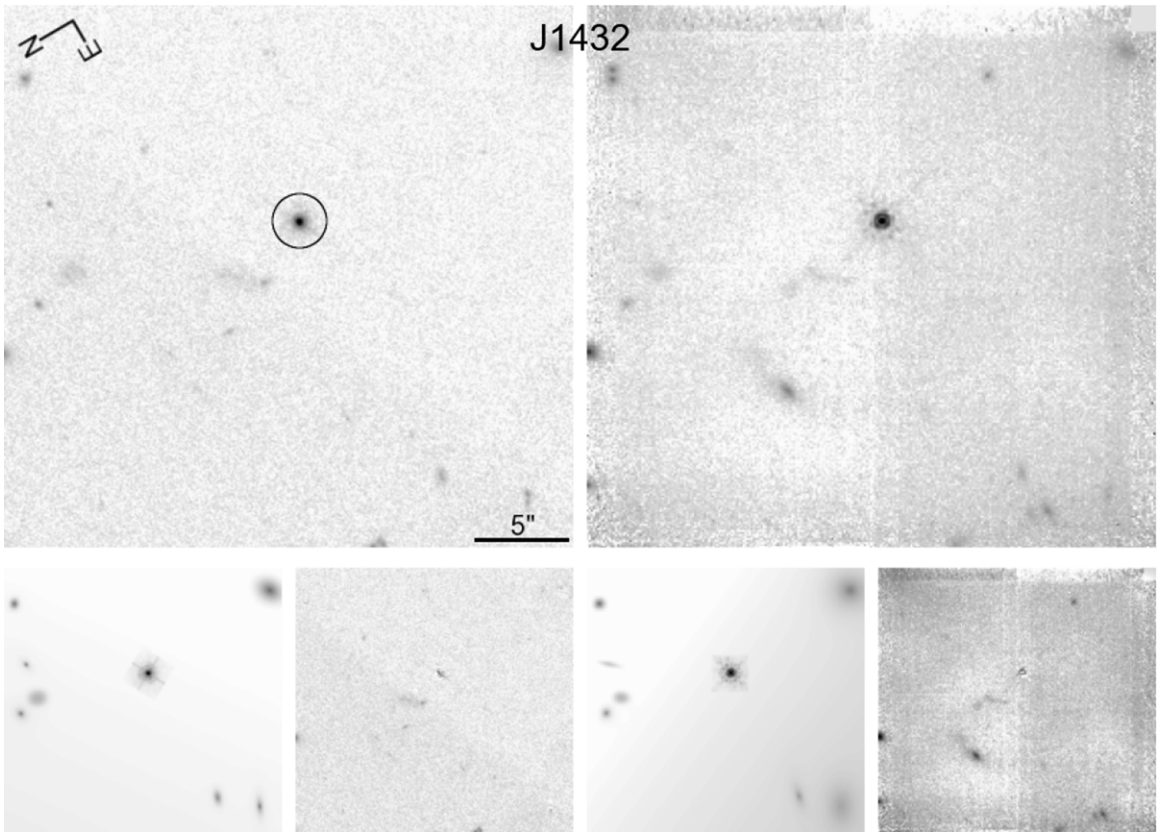

Figure 4. Same as Figure 1, but for J1432.

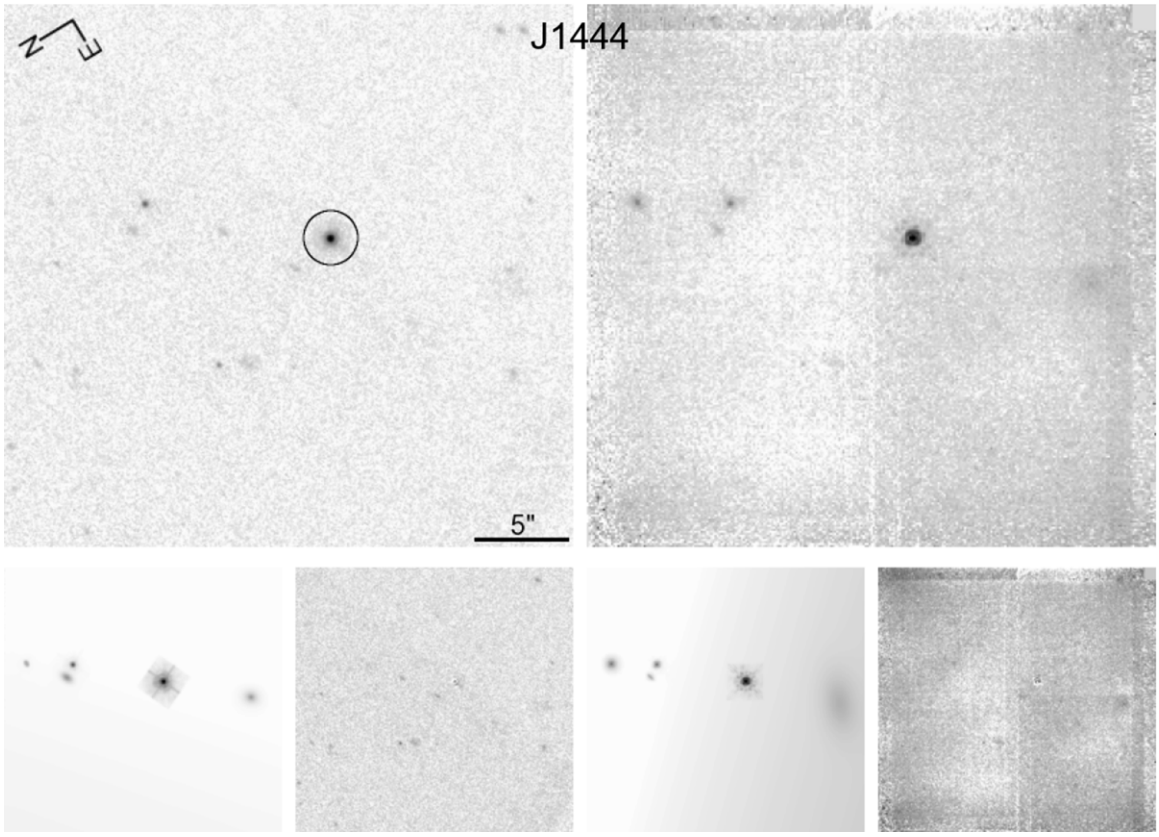

Figure 5. Same as Figure 1, but for J1444.

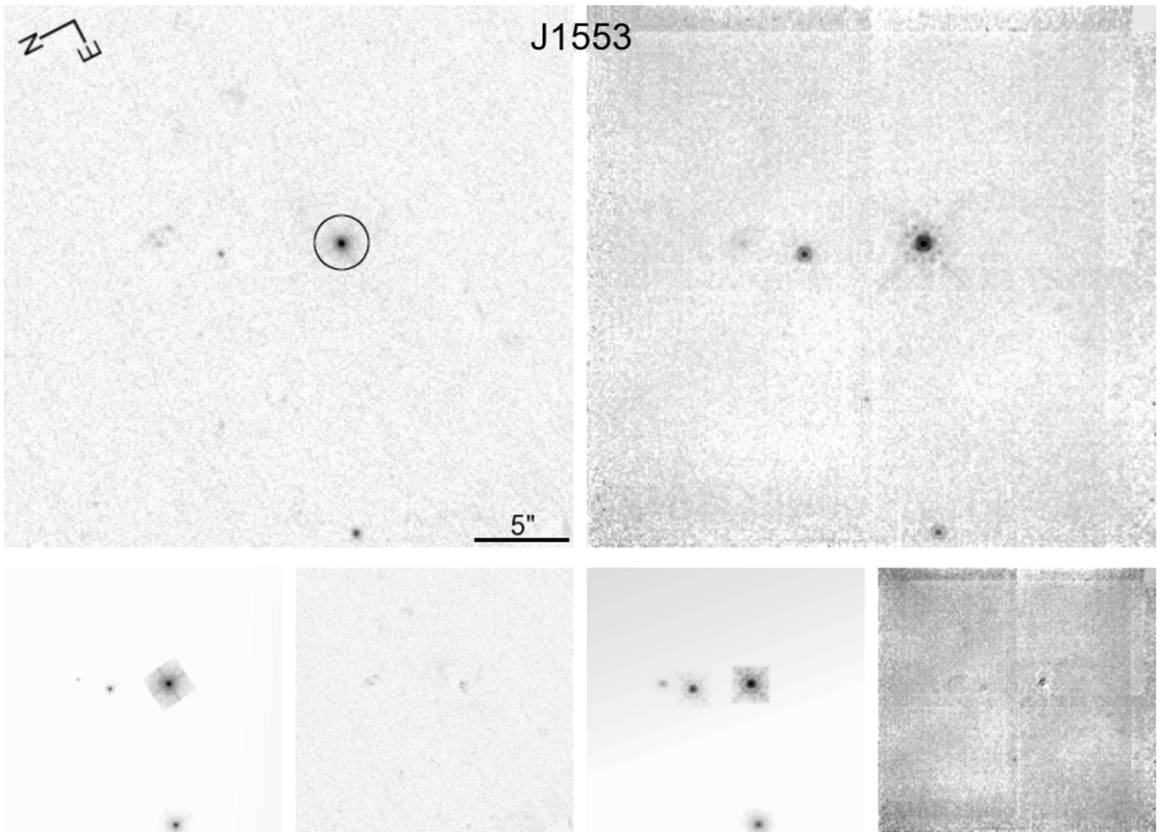

Figure 6. Same as Figure 1, but for J1553.

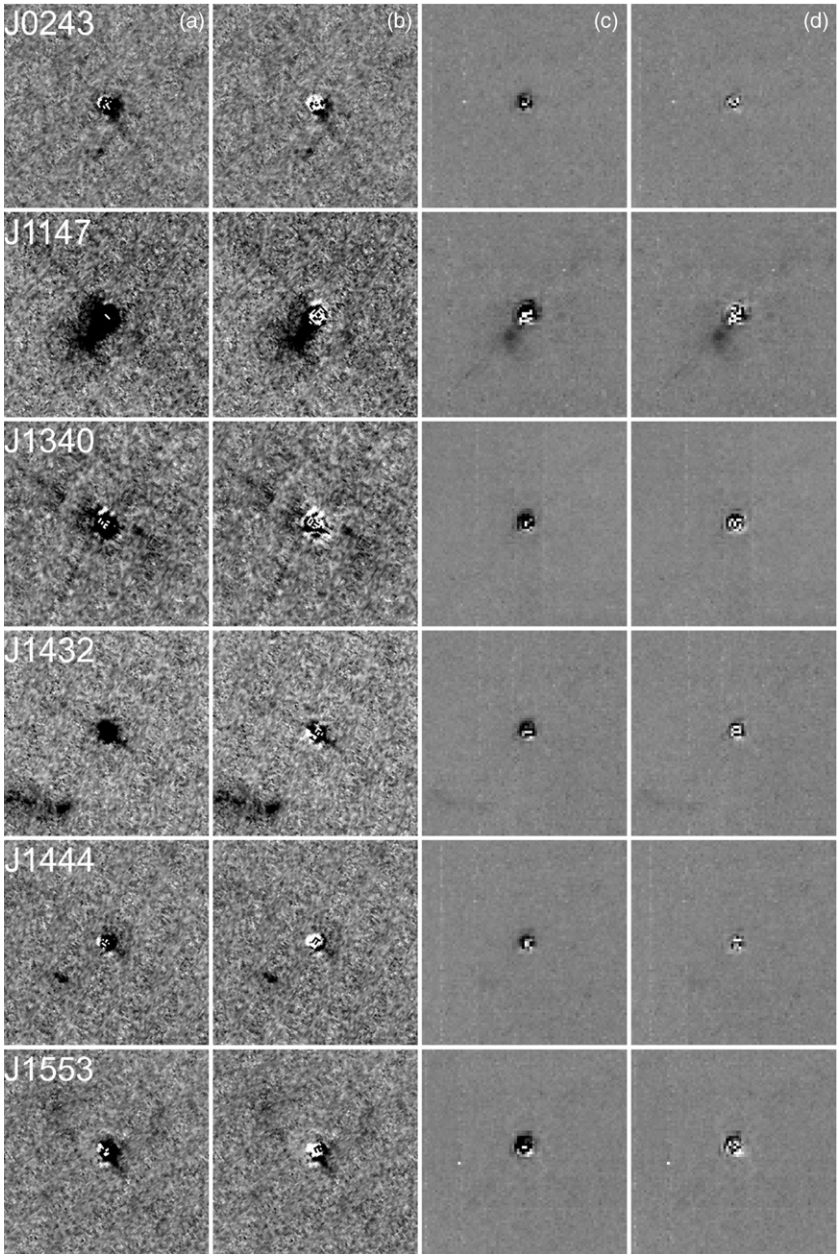

Figure 7. Details of the PSF subtraction for each object. Each panel is $6'' \times 6''$, and each object is shown at the same orientation as it was previously presented. All the ACS images have the same color scale, and the NICMOS images all have the same color scale. For each object, the panels are as follows: (a) ACS F625W image, with the best-fit PSF subtracted; (b) ACS F625W image with the best-fit PSF + Sérsic combination subtracted; (c) NIC2 F160W image with the best-fit PSF subtracted; (d) NIC2 F160W image with the best-fit PSF + Sérsic combination subtracted.

better fit was achieved with the addition of a compact (Sérsic 1968) profile, which has the form

$$\Sigma(r) = \Sigma_e \exp^{-\kappa[(r/r_e)^{1/n}-1]} \quad (1)$$

where r_e is the effective radius of the component, Σ_e is the surface brightness at r_e, n is the power-law index, and κ is coupled to n such that half of the total flux is within r_e. Two special cases of the Sérsic function are the exponential profile ($n = 1$), often used in modeling galactic disks, and the de Vaucouleurs (1948) profile ($n = 4$), historically used for modeling galactic bulges. Table 2 lists the integrated magnitudes and best-fit parameters of the PSF and Sérsic fits to each of the targets in the ACS and NICMOS images. Figure 7 compares the residuals after subtracting a single PSF component from each image to the residuals after subtracting a PSF component plus a Sérsic component.

In addition, we also fit any field objects that were visible in both the ACS and NICMOS images of each source. The NIC2 field of view is much smaller than that of the WFC, therefore, only objects that were $\lesssim$15 arcsec from each target were included. Table 3 lists the fit parameters determined for the field objects. The models and the fit residuals are shown in the bottom panels of Figures 1–6.

4. DISCUSSION

While the fits to the images were statistically improved by the addition of a Sérsic component to the PSF model produced by TinyTim, it is unlikely that these Sérsic components represent

Table 2
Fit Parameters for LBG Candidates

Object	PSF	Sérsic component					Additional component				
	m[a] (stmag)	m (stmag)	Δd[b] (arcsec)	r_e (kpc)	n	b/a[c]	m (stmag)	Δd (arcsec)	r_e (kpc)	n	b/a
					ACS WFC F625W						
J0243	21.88	21.19	0.04	0.26	1.0	0.12					
J1147	21.37	20.92	0.06	0.26	4.5	0.79	23.10	0.78	6.47	0.96	0.64
J1340	20.72	20.25	0.04	0.12	4.8	0.65					
J1432	22.44	20.31	0.05	0.01	14.2	0.49					
J1444	21.44	22.16	0.04	0.39	1.0	0.57					
J1553	22.11	20.83	0.03	0.31	2.8	0.48					
					NIC2 F160W						
J0243	22.69	23.03	0.04	0.40	1.0	0.85					
J1147	20.59	23.38	0.17	1.71	1.0	0.24	23.19	0.77	6.86	1.9	0.71
J1340	22.06	21.68	0.03	0.87	0.01	0.69					
J1432	21.88	23.31	0.08	0.68	3.2	0.73					
J1444	22.23	24.08	0.06	1.02	1.0	0.75					
J1553	21.66	22.19	0.09	0.51	1.0	0.68					

Notes.
[a] Magnitudes are presented in the STMAG system, which is defined such that Vega has a constant flux per unit wavelength and has the form $m = -2.5 \log f_\lambda - 21.10$.
[b] Distance from the center of the component to the center of the PSF.
[c] Ratio of the semi-major axis to the semi-minor axis for the component.

Table 3
Fit Parameters for Field Objects

Field	Function	ACS HRC F625W					NIC2 F160W				
		Δd (arcsec)	m_{F625W} (mag)	r_e (arcsec)	n	b/a	Δd (arcsec)	m_{F160W} (mag)	r_e (arcsec)	n	b/a
J1147	Sérsic	4.71	23.86	1.04	0.36	0.16	4.51	25.27	0.50	0.37	0.13
	Sérsic	6.80	23.53	0.88	0.25	0.26	6.76	24.28	0.29	1.0	0.32
J1340	Sérsic	4.28	23.51	0.88	1.8	0.37	4.00	24.33	0.45	0.47	0.54
	Sérsic	4.47	24.17	0.14	1.2	0.67	4.45	26.35	0.12	0.25	0.31
	Sérsic	4.70	25.94	0.11	1.9	0.44	4.65	25.50	2.0	1.6	0.35
J1432	Sérsic	8.57	24.29	0.43	0.45	0.82	8.53	25.20	0.36	0.45	0.70
	Sérsic	9.24	24.82	0.37	20	0.56	9.28	25.76	0.68	0.97	0.18
	Sérsic	10.1	24.59	0.22	5.0	0.81	9.94	25.07	0.26	3.5	0.84
	Sérsic	10.7	24.69	0.28	1.1	0.50	10.7	24.32	1.1	2.9	0.33
	Sérsic	11.2	22.52	0.44	1.2	0.76	11.0	22.15	1.2	1.7	0.95
	Sérsic	11.4	24.42	0.16	1.1	0.81	11.3	24.20	0.22	3.3	0.94
	Sérsic	13.1	24.49	0.34	2.9	0.32	13.2	22.76	1.5	0.94	0.64
J1444	Sérsic	6.73	25.58	0.33	2.3	0.84	7.29	22.84	1.9	0.73	0.54
	Sérsic	6.96	24.60	0.040	0.72	0.84	6.87	25.41	0.068	2.4	0.90
	Sérsic	7.31	25.64	0.22	0.93	0.11	7.25	26.61	0.17	0.32	0.27
	Sérsic	10.4	27.00	0.20	0.020	0.57	10.3	23.65	1.4	8.1	0.95
J1553	PSF	4.45	25.22	...	...	...	4.41	23.43	...	...	...
	Sérsic	...	...	...	...	...	4.46	24.83	0.11	0.020	0.34
	Sérsic	6.85	25.22	0.00050	0.39	0.10	6.69	26.31	0.17	1.1	0.61
	Sérsic	10.7	23.35	0.039	0.042	0.66	10.6	23.48	2.4	6.3	0.90
	Sérsic	...	...	...	...	...	10.6	24.44	0.013	0.82	0.90

a separate flux component, and are more likely due to PSF mismatches between the data and the models. Indeed, for J0243, J1444, and J1553, the extra flux component attributed to the Sérsic profile lies on the right-hand side of the PSF in the unrotated ACS image. This is also true of the NICMOS images presented in Figure 7, where the PSF mismatch is most apparent along the top edge of the PSF model for not only these three, but all six objects.

Rather, it appears that the only object with a significant contribution of flux from a galaxy component is J1147, which has a faint galaxy companion centered ~ 0.8 arcsec southwest of the PSF. Although it is obviously visible in the images, this additional component only contributes $\sim$8% of the flux to both the observed-frame optical and infrared. While it does have a similar $r - H$ color to J1147, -0.09 and -0.13, respectively, with such limited information it is impossible to know whether this object is at the same redshift as J1147.

In addition, there is also no evidence to support the lensing hypothesis for these objects. The fields around them are fairly empty for the most part. J1432 has a modest overdensity of objects, but there are no lensing artifacts, such as arcs or rings, present in either the ACS or NICMOS images of this object.

From the fact that all of these objects (with the possible exception of J1147) are unresolved point sources in both deep

optical and infrared images at the resolution of *HST*, it appears that these objects are unusual AGNs. Indeed, this is consistent with the findings of Appenzeller et al. (2005), who acquired an echelle spectrum of J1553 on the VLT and found that it was a broad absorption line quasar mimicking a Lyman break galaxy through the combination of absorption lines with relatively moderate widths and unfortunately located metal lines from an intervening system. They identify J1553 as most likely being a member of the rare iron low-ionization broad absorption line (FeLoBAL) quasar class. But even for this class of objects, J1553 is still an oddity. Furthermore, near-infrared spectroscopy by Ivison et al. (2005) shows that each of the objects has a very broad Hα emission line, which is a clear sign of AGN activity. Finally, Ivison et al. were unable to detect any of the six objects in the submillimeter, indicating that they cannot possibly have the high SFRs that would naturally accompany such luminous objects if they were bona fide LBGs.

5. SUMMARY

We have presented high-resolution *HST* follow-up images of the six bright Lyman break galaxy candidates that were previously identified in the Sloan Digital Sky Survey. We find that, with the exception of J1147, they are all consistent with unresolved point sources in both the rest-frame UV and optical. They are most likely members of the LoBAL quasar class, and possibly the even rarer FeLoBAL class, although their spectral properties are atypical of both classes of objects.

In the case of J1147, an additional flux component has been identified, located a mere $\sim$0.8 arcsec SW of the PSF, but this component is only contributing 8% of the flux. Further study will be necessary to determine whether this object is located at the same redshift as J1147.

This work is based on observations with the NASA/ESA *Hubble Space Telescope*. We are grateful for support of this work through grant GO-10181 from the Space Telescope Science Institute, which is operated by the Association of Universities for Research in Astronomy, Inc., under NASA contract NAS5-26555.

REFERENCES

Abazajian, K., et al. 2003, AJ, 126, 2081
Adelberger, K. L., & Steidel, C. C. 2000, ApJ, 544, 218
Appenzeller, I., Stahl, O., Tapken, C., Mehlert, D., & Noll, S. 2005, A&A, 435, 465
Bentz, M. C., & Osmer, P. S. 2004, AJ, 127, 576
Bentz, M. C., Osmer, P. S., & Weinberg, D. H. 2004, ApJ, 600, L19
de Vaucouleurs, G. 1948, Ann. Astrophys., 11, 247
Ivison, R. J., Smail, I., Bentz, M., Stevens, J. A., Menéndez-Delmestre, K., Chapman, S. C., & Blain, A. W. 2005, MNRAS, 362, 535
Krist, J. 1993, in ASP Conf. Ser. 52, Astronomical Data Analysis Software and Systems II, ed. R. J. Hanisch, R. J. V. Brissenden, & J. Barnes (San Francisco, CA: ASP), 536–539
Peng, C. Y., Ho, L. C., Impey, C. D., & Rix, H.-W. 2002, AJ, 124, 266
Schechter, P. 1976, ApJ, 203, 297
Schneider, D. P., et al. 2002, AJ, 123, 567
Seitz, S., Saglia, R. P., Bender, R., Hopp, U., Belloni, P., & Ziegler, B. 1998, MNRAS, 298, 945
Sérsic, J. L. 1968, Atlas de Galaxias Australes (Cordoba, Argentina: Observatorio Astronomico)
Shapley, A. E., Steidel, C. C., Pettini, M., & Adelberger, K. L. 2003, ApJ, 588, 65
Stoughton, C., et al. 2002, AJ, 123, 485
York, D. G., et al. 2000, AJ, 120, 1579